Ultraefficient homogeneous catalyst for the CO_2-to-CO electrochemical conversion

Cyrille Costentin[1], Guillaume Passard, Marc Robert[1], and Jean-Michel Savéant[1]

Université Paris Diderot, Sorbonne Paris Cité, Laboratoire d'Electrochimie Moléculaire, Unité Mixte de Recherche Université—Centre National de la Recherche Scientifique, 75205 Paris Cedex 13, France

Contributed by Jean-Michel Savéant, August 31, 2014 (sent for review August 9, 2014; reviewed by Harry B. Gray and Alain Deronzier)

A very efficient electrogenerated Fe^0 porphyrin catalyst was obtained by substituting in tetraphenylporphyrin two of the opposite phenyl rings by *ortho*-, *ortho*'-phenol groups while the other two are perfluorinated. It proves to be an excellent catalyst of the CO_2-to-CO conversion as to selectivity (the CO faradaic yield is nearly quantitative), overpotential, and turnover frequency. Benchmarking with other catalysts, through catalytic Tafel plots, shows that it is the most efficient, to the best of our knowledge, homogeneous molecular catalyst of the CO_2-to-CO conversion at present. Comparison with another Fe^0 tetraphenylporphyrin bearing eight *ortho*-, *ortho*'-phenol functionalities launches a general strategy where changes in substituents will be designed so as to optimize the operational combination of all catalyst elements of merit.

solar fuels | CO_2 reduction | electrochemistry | catalysis | contemporary energy challenges

The reductive conversion of CO_2 to CO is an important issue of contemporary energy and environmental challenges (1–10). Several low-oxidation-state transition metal complexes have been proposed to serve as homogeneous catalyst for this reaction in nonaqueous solvents such as N,N'-dimethylformamide (DMF) or acetonitrile (11–23).

Among them, electrochemically generated Fe^0 complexes have been shown to be good catalysts, provided they are used in the presence of Brönsted or Lewis acids (17–19). More recent investigations have extended the range of Brönsted acids able to boost the catalysis of the CO_2-to-CO conversion by electrogenerated Fe^0TPP (Scheme 1) without degrading the selectivity of the reaction. They have also provided a detailed analysis of the reaction mechanism (24, 25).

This is notably the case with phenol, which gave rise to the idea of installing prepositioned phenol groups in the catalyst molecule as pictured in Scheme 1 under the heading "CAT." The result was indeed a remarkably efficient and selective catalyst of the CO_2-to-CO conversion (26). At first blush, the comparison with the role of phenol in the case of FeTPP would entail attributing this considerable enhancement of catalysis to a local concentration of phenol much larger than can be achieved in solution. In fact, as analyzed in detail elsewhere (27), the role played by the internal phenol moieties is twofold. They indeed provide a very large local phenol concentration, favoring proton transfers, but they also considerably stabilize the initial Fe^0–CO_2 adduct through H bonding. Although the favorable effect of pendant acid groups has been noted in several cases (see ref. 27 and references therein), this was, to our knowledge, the first time their exact role was deciphered. The difference in the role played by the phenol moieties takes place within the framework of two different mechanisms (see Scheme 2 for CAT and FCAT and Scheme 3 for FeTPP) (27). With FeTPP, the first step is, as with CAT and FCAT, the addition of CO_2 on the electrogenerated Fe^0 complex (et_1 in Schemes 2 and 3). The strong stabilization of the Fe^0–CO_2 adduct formed according to reaction 1 (in Schemes 2 and 3) in the latter cases compared with the first has a favorable effect on catalysis, but one consequence of this stabilization is that catalysis then required an additional proton (reactions 2_1 and 2_2 in Scheme 2), the final, catalytic loop-closing step being the cleavage of one of the C–O bonds of CO_2 concerted with both electron transfer from the electrode and proton transfer from one of the local phenol groups (et_2 in Scheme 2). In the FeTPP case, the C–O bond-breaking step (reaction 2 in Scheme 3) is different: it involves an intramolecular electron transfer concerted with proton transfer and cleavage of the C–O bond. The catalytic loop is closed by a homogeneous electron transfer step (et_2 in Scheme 3) that regenerates the initial Fe^I complex.

The object of the present contribution is to test the idea that introduction of different substituents on the periphery of the porphyrin ring may improve the efficiency of the catalysis of CO_2-to-CO conversion. In such a venture, we will have to take into account both the overpotential at which the reaction takes place and the catalytic rate expressed as the turnover frequency as detailed in the following sections. Taking these two aspects simultaneously into consideration is essential in view of the possibility that substitution may improve one of the two factors and degrade the other, or vice versa. As a first example, we examined the catalytic performances of the FCAT molecule (Scheme 1), in which four of the eight phenol groups have been preserved in the same *ortho*-, *ortho*'- positions on two of the opposite phenyl rings, while the two other phenyl rings have been perfluorinated (the synthesis and characterization of this molecule is described in *SI Text*). A query that first comes to mind is as follows. The inductive effect of the fluorine atoms is expected to ease the reduction of the molecule to the Fe^0 oxidation state, and thus to be favorable to catalysis in terms of overpotential. However, will this benefit be blurred by a decrease of its reactivity toward CO_2? Indeed, the

Significance

Conversion of CO_2 into liquid fuels is one of the most important contemporary energy and environmental challenges. As a first step in this direction, the electrochemical reduction of CO_2 to CO requires catalysts, usually derived from transition metal complexes. In this paper, a very efficient, electrogenerated iron-porphyrin catalyst was obtained by introducing both pendant acid groups and fluorine substituents in the molecule. The former stabilize the CO_2-catalyst key intermediate via H bonding and provide a high local proton concentration. The latter help decrease the energy required to drive catalysis. Benchmarking this molecule with other catalysts shows that it is at present the most efficient, to the best of our knowledge, homogeneous molecular catalyst of the CO_2-to-CO conversion in terms of selectivity, overpotential, and turnover frequency.

Author contributions: C.C., M.R., and J.-M.S. designed research; G.P. performed research; C.C., G.P., M.R., and J.-M.S. analyzed data; and C.C., M.R., and J.-M.S. wrote the paper.

Reviewers: H.B.G., California Institute of Technology; and A.D., Centre National de la Recherche Scientifique.

The authors declare no conflict of interest.

[1]To whom correspondence may be addressed. Email: saveant@univ-paris-diderot.fr, cyrille.costentin@univ-paris-diderot.fr, or robert@univ-paris-diderot.fr.

This article contains supporting information online at www.pnas.org/lookup/suppl/doi:10.1073/pnas.1416697111/-/DCSupplemental.

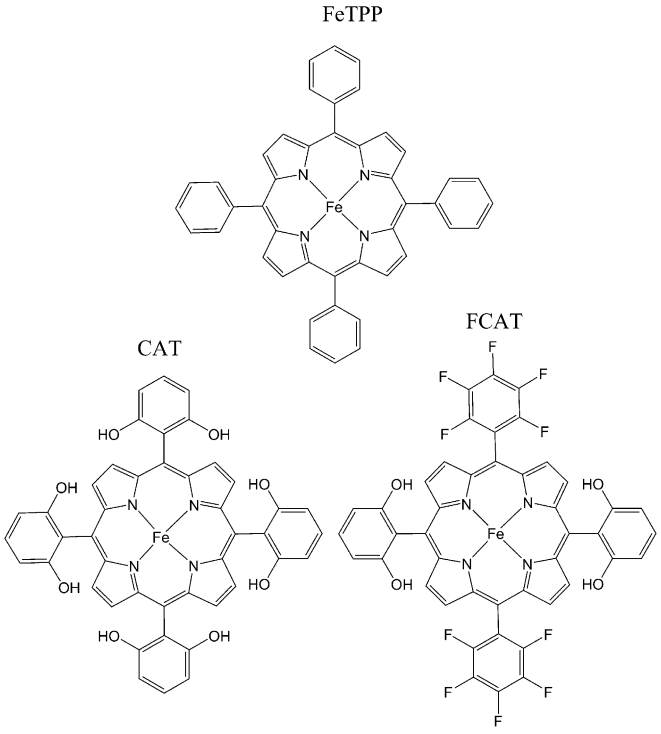

Scheme 1. Iron-based catalysts for CO_2-to-CO reduction.

same inductive effect of the fluorine atoms tends to decrease the electronic density on the Fe^0 complex and might therefore render the formation of the initial Fe^0-CO_2 adduct less favorable. Change in the rates of the follow-up reactions of Scheme 1 may also interfere. A first encouraging indication that the fluorine substitution has a globally favorable effect on catalysis derives from the comparison of the cyclic voltammetric responses of FCAT and CAT as represented in Fig. 1: the peak potential is slightly more positive for FCAT [−1.55 V vs. normal hydrogen electrode (NHE)] than for CAT (−1.60 V vs. NHE), whereas the apparent number of electrons at the peak at 0.1 V/s is clearly larger in the first case than in the second (120 vs. 80) (26). However, a deeper analysis of the meaning of these figures in terms of effective catalysis is

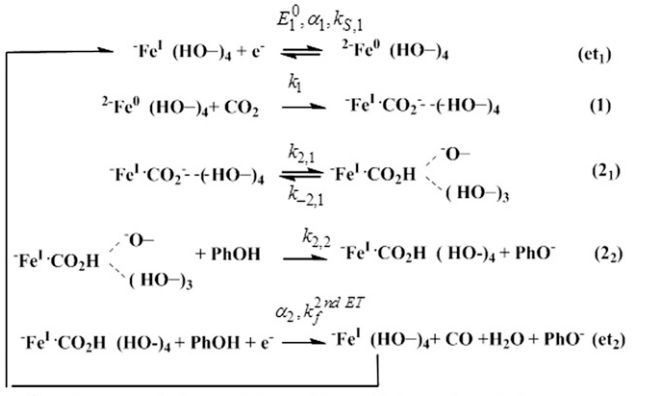

$E_1^0, \alpha_1, k_{S,1}$: standard potential, transfer coefficient and standard rate constant of the first electrode electron transfer, respectively. The k's are the homogeneous rate constants of the various reactions. $\alpha_2, k_f^{2nd\ ET}$: transfer coefficient and forward rate constant, respectively of the second electrode electron transfer

Scheme 2. Mechanism for the reduction of CO_2 with CAT and FCAT.

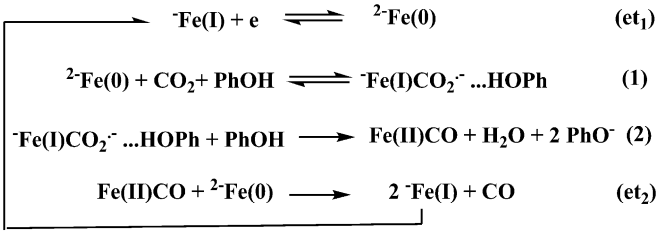

Scheme 3. Mechanism for the reduction of CO_2 with FeTPP.

required. The mechanism of the reaction (Scheme 2) has been shown to be the same with FCAT as with CAT, and the various kinetic parameters indicated in Scheme 2, whose values are recalled in Table 1, have been determined (26, 27). Comparison of the two catalysts may then be achieved more rationally based on the determination, in each case, of the catalytic Tafel plots, which relates the turnover frequency (*TOF*) to the overpotential (η). The latter is defined, in the present case of reductive processes, as the difference between the apparent standard potential of the CO_2/CO conversion, $E^0_{CO_2/CO}$ and the electrode potential, E:

$$\eta = E - E^0_{CO_2/CO}.$$

Large catalytic currents correspond to "pure kinetic conditions" in which a steady state is achieved by mutual compensation of catalyst transport and catalytic reactions. The cyclic voltammetry (CV) responses are then S-shaped independent of scan rate. They are the same with other techniques such as rotating disk electrode voltammetry and also during preparative-scale electrolyses. The fact that peaks instead of plateaus are observed at low

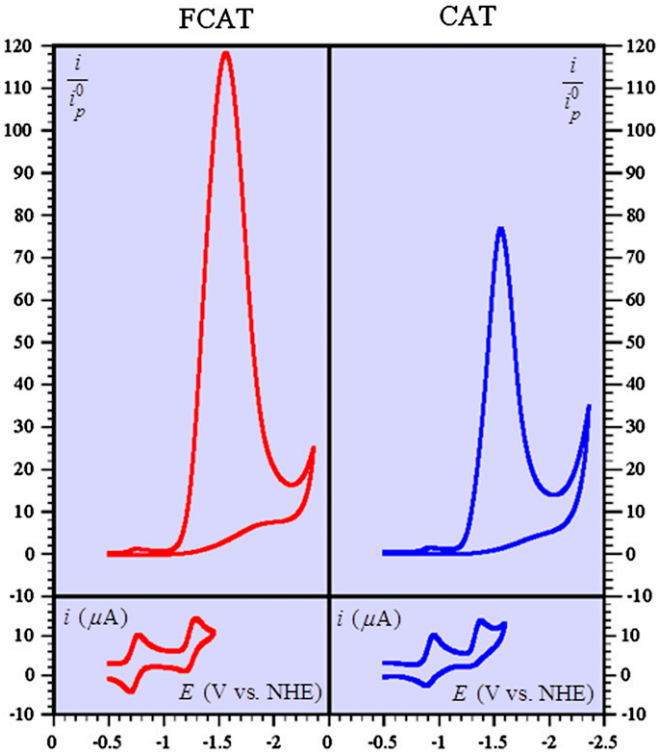

Fig. 1. CV of 1-mM FCAT (*Lower Left*) and CAT (*Lower Right*) in neat DMF + 0.1 M n-Bu_4NPF_6 at 0.1 Vs^{-1}. The same, *Upper Left* and *Upper Right*, respectively, in the presence of 0.23 M CO_2 and of 1 M PhOH. i_p^0, the peak current of the reversible Fe^{II}/Fe^{I} wave is a measure of a one-electron transfer.

CHEMISTRY

Table 1. Kinetic characteristics of the reactions in Scheme 2 from ref. 27

Parameters for catalysis	FCAT	CAT
$k_1(M^{-1}\cdot s^{-1})$	3×10^5	$>5 \times 10^6$
$(k_{21}/k_{-21})k_{22}(M^{-1}\cdot s^{-1})$	2.5×10^4	—
$k_{21}(s^{-1})$	3×10^4	7×10^3
$k_2^{ap}(s^{-1})$	2.1×10^4	7×10^3
α_2	0.3	
[PhOH] (M)	$\log k_f^{2nd\ ET}$ (cm s^{-1})	
0.3	−8.8	−9.4
0.5	−8.8	−9.4
1	−8.6	−9.3
2	−8.4	−9.0
3	−8.25	−8.8

The k_2^{ap} value for FCAT is given for [PhOH] = 3 M. It is independent from the acid concentration in the case of CAT.

scan rate, as in Fig. 1, derives from secondary phenomena related to the observed high catalytic efficiencies, such as substrate consumption, inhibition by products, and deactivation of the catalyst. These factors and the ways to go around their occurrence to finally obtain a full characterization of the mechanism and kinetics of the catalysis process are discussed in detail elsewhere (27). Under pure kinetic conditions, the active catalyst molecules are then confined within a thin reaction-diffusion layer adjacent to the electrode surface. During the time where the catalyst remains stable, the *TOF* is defined as

$$TOF = N_{product}/N_{active\ cat},$$

where $N_{product}$ is the number of moles of the product, generated per unit of time, and $N_{active\ cat}$ is the maximal number of moles of the active form catalyst contained in the reaction–diffusion layer rather than in the whole electrochemical cell (for more information on the notions of pure kinetic conditions, reaction–diffusion layer, and on the correct definition of *TOF*, see refs. 23, 26, 28). For the present reaction mechanism (Scheme 2) as well as for all reaction schemes belonging to the same category, the *TOF*–η relationships are obtained from the following equations (28, 29), using the notations defined in Scheme 2 and the data listed in Table 1.

$$TOF = \frac{TOF_{\max}}{\left\{1 + \frac{i_{pl}}{2FSC_{cat}^0 k_f^{2nd\ ET}}\exp(\alpha_2 fE) + \frac{i_{pl}}{2FSC_{cat}^0\sqrt{D_{cat}}\sqrt{k_1[CO_2]}}\exp\left[\frac{F}{RT}\left(E - E_1^0\right)\right]\right\}},$$

with

Table 2. Comparison of FCAT and CAT with other catalysts of the CO_2/CO conversion

Reference	Solvent + acid $E^0_{CO_2/CO}$	Catalyst E^0_{cat}	$k_1^{ap}[CO_2]$ k_2^{ap}	logTOF_{max} (s^{-1})	logTOF_0 (s^{-1})*
27; this work	DMF +3 M PhOH −0.69	CAT −1.35	$>5 \times 10^6$ See Table 1	3.8	−6.0
27; this work	DMF +3 M PhOH −0.69	FCAT −1.28	$>5 \times 10^6$ See Table 1	4.0	−5.5
25	DMF +3 M PhOH −0.69	Fe^0TPP −1.43	3.5×10^4 †	4.5	−8.0
21	DMF +0.1 M HBF_4 −0.23	m-$(triphos)_2Pd_2$‡ −0.76	35 †	1.5	−7.4
20	CH_3CN +0.8 M CF_3CH_2OH -0.65	Re(bpy)$(CO)_3$(py) −1.30	875 †	2.9	−8.0
12	CH_3CN +1.4 M CF_3CH_2OH -0.65	Mn(bpytBu)$(CO)_3Br$§ −1.40	680 †	2.8	−9.8
22	CH_3CN −0.65	$Ru^{II}(tpy^-)(bpy^-)$§ −1.34	7.6 †	0.9	−10.8
22	CH_3CN −0.65	$Ru^{II}(tpy^-)$(Mebim-py^-)§ −1.34	59 †	1.8	−9.9
23	CH_3CN −0.65	N_2 = $Mn(CO)_3$¶ −1.28	5×10^3 †	3.7	−7.0

Potentials in V vs. NHE, first-order or pseudo-first-order rate constants in s^{-1}.

**TOF* at $\eta = 0$.

†$k_2^{ap} >> k_1^{ap}[CO_2]$.

‡

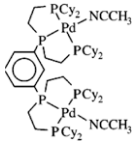

§py = pyridine, tpy = 2,2′:6′,2′′-terpyridine, bpy =2,2′-bipyridine, Mebimpy = 2,6-bis(1-methyl benzimidazol-2-yl)pyridine.

¶

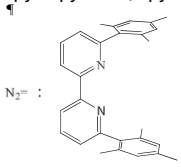

$$TOF_{\max} = \frac{1}{\frac{1}{k_1[CO_2]} + \frac{1}{k_2^{ap}}},\ k_2^{ap} = \frac{k_{21}k_{22}[PhOH]}{k_{-21} + k_{22}[PhOH]}.$$

The S-shaped catalytic wave is characterized by a plateau current i_{pl} that may be expressed as

$$i_{pl} = \frac{2FS\sqrt{D_{cat}}C^0_{cat}\sqrt{k_1[CO_2]}}{1 + \frac{\sqrt{k_1[CO_2]}}{\sqrt{k_{2,ap}}\left(1 + \frac{\sqrt{k_{2,ap}}}{\sqrt{k_1[CO_2]}}\right)}\left[1 + \frac{k_{2,ap}}{k_{2,2}C^0_Z}\right]}, \quad [1]$$

where S is electrode surface area; C^0_{cat} and D_{cat} are concentration and diffusion coefficient of the catalyst, respectively.

The logTOF–η plots (Fig. 2) move upward as the phenol concentration increases. They are more favorable for FCAT than for CAT whatever [PhOH]. A more direct comparison between the two catalysts at [PhOH] = 3 M is shown in Fig. 3, where the results of preparative-scale electrolyses are also displayed within the same logTOF vs. η framework, pointing to the superiority of FCAT over CAT. This is confirmed by preparative-scale electrolyses. Fixed-potential electrolyses were performed at −1.08 and −1.14 V vs. NHE with 1 mM FCAT and CAT, respectively, using a carbon crucible as working electrode under 1 atm. CO_2 (0.23 M) in the presence of 3 M PhOH. The current density i_{el}/S_{el} is stable over 3 h with FCAT and 0.5 h with CAT and the production of CO is practically quantitative (faradaic yields of 100 ± 10% and 100 ± 5%, respectively, less than 1% H_2 in both cases). i_{el}/S_{el}= 0.5 and 0.3 mA/cm^2 with FCAT and CAT, respectively; S_{el}, the working electrode surface area of the preparative-scale electrode electrolysis, is much larger (20 cm^2) than in CV experiments (0.07 cm^2). The corresponding TOF value at the operated overpotential is calculated from $TOF = (i_{el}/i_{pl})TOF_{\max}$, in which i_{pl} is the plateau current given by Eq. **1**. The TOF values thus obtained are 240 s^{-1} (at η = 0.39 V) and 170 s^{-1} (at η = 0.45 V) for FCAT and CAT, respectively. As seen in Fig. 3, they satisfactorily match the TOF–η relationships derived from CV taking into account inevitable imperfections in cell configuration leading to residual ohmic drop. Besides catalytic performances evaluated through logTOF–η relationship, durability is important in the evaluation of catalyst efficiency. It has been evaluated through estimation of the catalyst degradation over prolonged electrolysis. This estimation is based on recording CVs in the electrolysis solution during electrolysis. It turns out that (see *SI Text* for details) FCAT is more stable than CAT or simple FeTPP. Complete degradation of the initial 10^{-5} moles of catalyst is observed after the passage of 575, 200, and 290 coulombs for FCAT, CAT, and simple FeTPP, corresponding to 600, 210, and 300 catalytic cycles for FCAT, CAT and FeTPP, respectively.

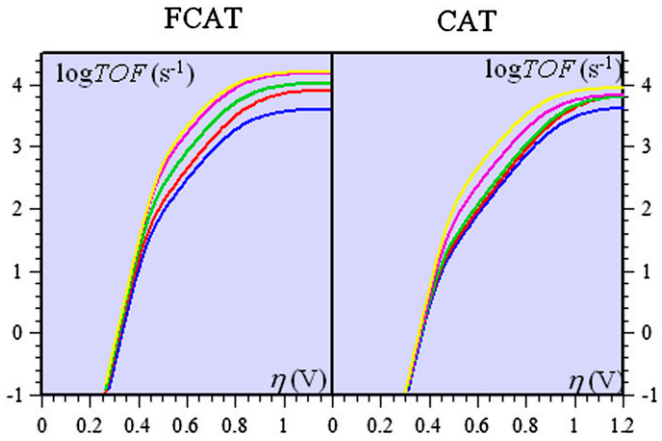

Fig. 2. Catalytic Tafel plots for the two catalysts (see text) as a function of the concentration of phenol in the solution, in M, from bottom to top: 0.3, 0.5, 1, 2, 3.

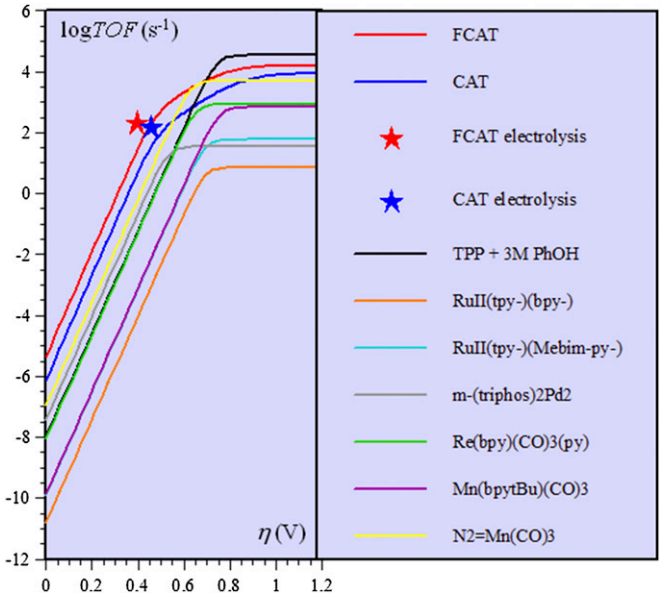

Fig. 3. Benchmarking of all catalysts based on catalytic Tafel plots derived from CV experiments. See Table 2.

How do these modified Fe^{0}TPP catalysts compare with other catalysts of the CO_2/CO conversion described in the literature? Table 2 summarizes the various parameters that we could extract from previous reports as detailed in *SI Text*. Fig. 3 illustrates the ensuing benchmarking of all catalysts. In terms of preparative-scale electrolyses, the available information indicates that the stability of the catalysts is of the same order as for the two catalysts FCAT and CAT described here.

Our conclusion is twofold. (*i*) The title iron porphyrin generated electrochemically under its Fe^0 form (FCAT) operated in the presence of 3 M phenol in DMF appears to be the best homogeneous catalyst of the CO_2-to-CO conversion to date. This clearly appears after benchmarking of presently available catalyst of this reaction under the form of catalytic Tafel plots relating turnover frequency with overpotential (Fig. 3). Such plot allows optimization of the catalytic reaction by appropriately compromising between rapidity and energy costs. A further advantageous feature of FCAT is that it relies on one of the cheapest and most earth-abundant metals. (*ii*) Fluorine substitution in passing from CAT to FCAT was designed to favor catalysis in terms of overpotential thanks to the inductive effect of the fluorine substituents. At the same time it could have rendered the follow-up reactions less favorable, possibly annihilating the initial favorable effect of fluorine sub or even making catalysis globally less efficient than with CAT. The observation that this is not the case, and that the substitution has a global positive effect in this case, opens the route to the design and testing of further substituted molecules, which could become even more efficient catalysts of the CO_2/CO conversion. It should be particularly fruitful to use the prepositioned phenol functionalities to favor the formation and proton-coupled transformation of the initial Fe^0–CO_2 adduct and to play with electron withdrawing substituents to improve the capabilities of the catalyst in terms of overpotential.

See *SI Text* for experimental details and data treatment of the other catalysts in Table 2.

ACKNOWLEDGMENTS. Partial financial support from the Agence Nationale de la Recherche (ANR 2010 BLAN 0808) is gratefully acknowledged.

1. Benson EE, Kubiak CP, Sathrum AJ, Smieja JM (2009) Electrocatalytic and homogeneous approaches to conversion of CO_2 to liquid fuels. *Chem Soc Rev* 38(1):89–99.
2. Rakowski DuBois M, DuBois DL (2009) Development of molecular electrocatalysts for CO_2 reduction and H_2 production/oxidation. *Acc Chem Res* 42(12):1974–1982.
3. Windle CD, Perutz RN (2012) Advances in molecular photocatalytic and electrocatalytic CO_2 reduction. *Coord Chem Rev* 256(21-22):2562–2570.
4. Savéant J-M (2008) Molecular catalysis of electrochemical reactions. Mechanistic aspects. *Chem Rev* 108(7):2348–2378.
5. Costentin C, Robert M, Savéant J-M (2013) Catalysis of the electrochemical reduction of carbon dioxide. *Chem Soc Rev* 42(6):2423–2436.
6. Schneider J, Jia H, Muckerman JT, Fujita E (2012) Thermodynamics and kinetics of CO_2, CO, and H^+ binding to the metal centre of CO_2 reduction catalysts. *Chem Soc Rev* 41(6):2036–2051.
7. Appel AM, et al. (2013) Frontiers, opportunities, and challenges in biochemical and chemical catalysis of CO_2 fixation. *Chem Rev* 113(8):6621–6658.
8. Aresta M, Dibenedetto A, Angelini A (2014) Catalysis for the valorization of exhaust carbon: From CO_2 to chemicals, materials, and fuels. technological use of CO_2. *Chem Rev* 114(3):1709–1742.
9. Smieja JM, et al. (2012) Kinetic and structural studies, origins of selectivity, and interfacial charge transfer in the artificial photosynthesis of CO. *Proc Natl Acad Sci USA* 109(39):15646–15650.
10. Oh Y, Hu X (2013) Organic molecules as mediators and catalysts for photocatalytic and electrocatalytic CO_2 reduction. *Chem Soc Rev* 42(6):2253–2261.
11. Bourrez M, Molton F, Chardon-Noblat S, Deronzier A (2011) [Mn(bipyridyl)$(CO)_3$Br]: An abundant metal carbonyl complex as efficient electrocatalyst for CO_2 reduction. *Angew Chem Int Ed Engl* 50(42):9903–9906.
12. Smieja JM, et al. (2013) Manganese as a substitute for rhenium in CO_2 reduction catalysts: The importance of acids. *Inorg Chem* 52(5):2484–2491.
13. Keith JA, Grice KA, Kubiak CP, Carter EA (2013) Elucidation of the selectivity of proton-dependent electrocatalytic CO_2 reduction by fac-Re(bpy)(CO)3Cl. *J Am Chem Soc* 135(42):15823–15829.
14. Froehlich JD, Kubiak CP (2012) Homogeneous CO_2 reduction by Ni(cyclam) at a glassy carbon electrode. *Inorg Chem* 51(7):3932–3934.
15. Hammouche M, Lexa D, Savéant J-M, Momenteau M (1988) Catalysis of the electrochemical reduction of carbon dioxide by iron("0") porphyrins. *J Electroanal Chem* 249: 347–351.
16. Hammouche M, Lexa D, Momenteau M, Savéant J-M (1991) Chemical catalysis of electrochemical reactions. Homogeneous catalysis of the electrochemical reduction of carbon dioxide by iron ("0") porphyrins. Role of the addition of magnesium cations. *J Am Chem Soc* 113:8455–8466.
17. Bhugun I, Lexa D, Saveant J-M (1994) Ultraefficient selective homogeneous catalysis of the electrochemical reduction of carbon dioxide by an iron(0) porphyrin associated with a weak Broensted acid cocatalyst. *J Am Chem Soc* 116:5015–5016.
18. Bhugun I, Lexa D, Saveant JM (1996) Catalysis of the electrochemical reduction of carbon dioxide by iron(0) porphyrins: Synergystic effect of weak Bronsted acids. *J Am Chem Soc* 118:1769–1776.
19. Bhugun I, Lexa D, Saveant JM (1996) Catalysis of the electrochemical reduction of carbon dioxide by iron(0) porphyrins. Synergistic effect of Lewis acid cations. *J Phys Chem* 100:19981–19985.
20. Wong K-Y, Chung W-H, Lau C-P (1998) The effect of weak Bronsted acids on the electrocatalytic reduction of carbon dioxide by a rhenium tricarbonyl bipyridyl complex. *J Electroanal Chem* 453:161–169.
21. Raebiger JW, et al. (2006) Electrochemical reduction of CO_2 to CO catalyzed by a bimetallic palladium complex. *Organometallics* 25:3345–3351.
22. Chen Z, et al. (2011) Electrocatalytic reduction of CO_2 to CO by polypyridyl ruthenium complexes. *Chem Commun (Camb)* 47(47):12607–12609.
23. Sampson MD, et al. (2014) Manganese catalysts with bulky bipyridine ligands for the electrocatalytic reduction of carbon dioxide: Eliminating dimerization and altering catalysis. *J Am Chem Soc* 136(14):5460–5471.
24. Costentin C, Drouet S, Robert M, Savéant J-M (2012) Turnover numbers, turnover frequencies, and overpotential in molecular catalysis of electrochemical reactions. Cyclic voltammetry and preparative-scale electrolysis. *J Am Chem Soc* 134(27): 11235–11242.
25. Costentin C, Drouet S, Passard G, Robert M, Savéant J-M (2013) Proton-coupled electron transfer cleavage of heavy-atom bonds in electrocatalytic processes. Cleavage of a C-O bond in the catalyzed electrochemical reduction of CO_2. *J Am Chem Soc* 135(24):9023–9031.
26. Costentin C, Drouet S, Robert M, Savéant J-M (2012) A local proton source enhances CO_2 electroreduction to CO by a molecular Fe catalyst. *Science* 338(6103):90–94.
27. Costentin C, Passard G, Robert M, Savéant J-M (2014) Pendant acid–base groups in molecular catalysts: H-bond promoters or proton relays? Mechanisms of the conversion of CO_2 to CO by electrogenerated iron(0)porphyrins bearing prepositioned phenol functionalities. *J Am Chem Soc* 136:11821–11829.
28. Savéant J-M (2006) *Elements of Molecular and Biomolecular Electrochemistry: An Electrochemical Approach to Electron Transfer Chemistry* (Wiley, Hoboken, NJ), pp 108–111.
29. Costentin C, Savéant J-M (2014) Multielectron, multistep molecular catalysis of electrochemical reactions: Benchmarking of homogeneous catalysts. *ChemElectroChem* 1: 1226–1236.

Supporting Information

Costentin et al. 10.1073/pnas.1416697111

SI Text

Experimental

Chemicals. N,N'-dimethylformamide (Acros, >99.8%, over molecular sieves); the supporting electrolyte was NBu_4PF_6 (Fluka, puriss.). All starting materials were obtained from Sigma-Aldrich, Fluka, and Alfa Aesar, used without further purification. $CHCl_3$ and CH_2Cl_2 were distilled from calcium hydride and stored under an argon atmosphere. ^1H NMR spectra were recorded on a Bruker Avance III 400-MHz spectrometer and were referenced to the resonances of the solvent used. The mass spectra were recorded on a Microtof-Q of Bruker Daltonics.

Synthesis and Characterization of Iron(III)5,15-bis(2′,6′-dihydroxyphenyl)-10,20-bis(pentafluorophenyl-Porphyrin. ***5-(Pentafluorophenyl) dipyrromethane (1).*** A solution of pentaflurobenzaldehyde (1 mL, 8.1 mmol) in freshly distilled (under vacuum) pyrrole (25 mL, 0.375 mol) was degassed by argon for 20 min, and then trifluoroacetic acid (60 μL, 0.81 mmol) was added. The mixture was stirred for 30 min at room temperature, then diluted with CH_2Cl_2 (200 mL) and washed with 0.1 M NaOH (200 mL). The organic layer was separated, washed with water and dried over Na_2SO_4, filtered, and the solvent was evaporated at reduced pressure to give brown solid. The residue was purified by column chromatography (silica gel, hexanes:ethyl acetate:triethylamine, 80:20:1) and then was purified by crystallization (water:ethanol, 90:10) to yield 5-(pentafluorophenyl)dipyrromethane as a white powder (1.15 g, 65%). ^1H NMR (400 MHz, $CDCl_3$): δ 5.90 (s, 1H, CH), 6.00–6.05 (m, 2H, ArH), 6.14–6.19 (m, 2H, ArH), 6.71–6.75 (m, 2H, ArH), 8.06 (s, 2H, NH).

5, 15-bis(2′,6′-dimethoxyphenyl)-10, 20-bis(pentafluorophenyl)-21H, 23H-porphyrin (1). To a solution of 5-(pentafluorophenyl)dipyrromethane (1g, 3.20 mmol) and 2,6-dimethoxybenzaldehyde (532 mg, 3.20 mmol) in dry chloroform (320 mL), previously degassed by argon for 20 min, was added $BF_3.OEt_2$ (149 μL, 1.21 mmol) by syringe. The solution was stirred at room temperature under inert atmosphere in the dark for 24 h, and 2,3-dichloro-5,6-dicyano-1,4-benzoquinone (DDQ) (543 mg, 2.40 mmol) was added to the solution. The mixture was stirred for an additional 24 h at room temperature; the solution was treated with a second portion of DDQ and refluxed for 2.5 h. The solvent was removed, and the resulting black solid was purified by column chromatography on silica gel using dichloromethane as eluent affording porphyrine **1** (445 mg, 30%) as a purple powder. ^1H NMR (400 MHz, $CDCl_3$): δ − 2.69 (s, 2H, NH), 3.53 (s, 12H, OCH_3), 7.02 (d, 4H, J = 8 Hz ArH), 7.77 (m, 4H, ArH), 8.70 (d, 4H, J = 4.8 Hz, $H_{\beta\text{-pyrolic}}$), 8.85 (d, 4H, J = 4.8 Hz, $H_{\beta\text{-pyrolic}}$). High resolution electrospray ionization-mass spectrum (HRESI-MS) ($[M+H]^+$) calculated for $C_{48}H_{29}F_{10}N_4O_4$ 915.1994, found 915.2024.

5, 15-bis(2′,6′-dihydroxyphenyl)-10, 20-bis(pentafluorophenyl)-21H, 23H-porphyrin (2). To a solution of porphyrin 1 (300 mg, 3.28×10^{-4} mol) in dry dichloromethane (20 mL) at −20 °C was added BBr_3 (315 μL, 3.28 mmol). The resulting green solution was stirred for 12 h at room temperature under inert atmosphere and then placed in ice water. Ethyl acetate was added to the suspension and the mixture was washed with $NaHCO_3$ until the solution became purple. The organic layer was separated, washed twice with water, filtered, and dried over anhydrous Na_2SO_4. The resulting solution was evaporated. The residue was purified by column chromatography (silica gel, dichloromethane) to yield porphyrin 2 as a purple powder (227 mg, 81%). ^1H NMR (400 MHz, $CDCl_3$): δ − 2.80 (s, 2H, NH), 6.97 (d, 4H, J = 8 Hz, ArH), 7.63 (t, 2H, J = 8 Hz, ArH), 8.87 (d, 4H, J = 4.4 Hz, $H_{\beta\text{-pyrolic}}$), 9.08 (d, 4H, J = 4.8 Hz, $H_{\beta\text{-pyrolic}}$). HRESI-MS ($[M+H]^+$) calculated for $C_{44}H_{21}F_{10}N_4O_4$ 859.1388, found 859.1398.

Chloro iron(III) 5,15-bis(2′,6′-dihydroxyphenyl)-10,20-bis(pentafluorophenyl)-porphyrin (3). A solution of compound **2** (100 mg, 1.16×10^{-4} mol), anhydrous iron (II) bromide (452 mg, 2.09 mmol), and 2,6-lutidine (34 μL, 2.9×10^{-4} mol) was heated at 50 °C and stirred 3 h under inert atmosphere in dry methanol. After methanol was removed, the resulting solid was dissolved in ethyl acetate, washed with 1.2 M HCl solution, and then washed until pH was neutral. The crude product was purified by column chromatography (silica gel, 90:10, dichloromethane–methanol) and obtained after a precipitation. The product is dissolved in a small quantity of CH_2Cl_2; a small amount of concentrated HCl was added with a large quantity of hexane to give compound **3** as a brown solid (108 mg, 98%). HRESI-MS ($[M]^+$) calculated for $C_{44}H_{18}FeF_{10}N_4O_4$ 912.0512, found 912.0513.

Cyclic Voltammetry. The working electrode was a 3-mm-diameter glassy carbon (Tokai) disk carefully polished and ultrasonically rinsed in absolute ethanol before use. The counterelectrode was a platinum wire and the reference electrode an aqueous SCE electrode. All experiments were carried out under argon or carbon dioxide at 21 °C, the double-wall jacketed cell being thermostated by circulation of water. Cyclic voltammograms were obtained by use of a Metrohm AUTOLAB instrument. Ohmic drop was compensated using the positive feedback compensation implemented in the instrument.

Preparative-Scale Electrolysis. Electrolyses were performed using a Princeton Applied Research (PARSTAT 2273) potentiostat. The experiments were carried out in a cell with a carbon crucible as working electrode ($S = 20$ cm^2); the volume of the solution is 10 mL The reference electrode was an aqueous SCE electrode and the counterelectrode a platinum grid in a bridge separated from the cathodic compartment by a glass frit, containing a 0.4 M $Et_4N^+,CH_3CO_2^-$ + 0.1 M NBu_4PF_6 N,N'-dimethylformamide solution. The role of $Et_4N^+,CH_3CO_2^-$ is to serve as reactant at the anode, producing CO_2 and ethane (Kolbe reaction). Some diffusion of these products toward the cathodic compartment is expected to have negligible effect on the yields of the cathodic reaction. The electrolysis solution was purged with CO_2 for 20 min before electrolysis for quantitative experiments and under a continuous flux for the long-time-scale electrolysis (to avoid the CO_2 consumption). The cell configuration was described elsewhere.

Ohmic drop was minimized as follows: the reference electrode is directly immerged in the solution (without separated bridge) and put progressively closer to the working electrode until oscillations appear. It is then slightly moved away until the remaining oscillations are compatible with recording of the catalytic current–potential curve. The appearance of oscillations in this cell configuration does not require positive feedback compensation as it does with microelectrodes. The potentiostat is equivalent to a self-inductance. Oscillations thus appear as soon as the resistance that is not compensated by the potentiostat comes close to zero as the reference electrode comes closer and closer to the working electrode surface.

Gas Detection. Gas chromatography analyses of gas evolved in the course of electrolysis were performed with an HP 6890 series equipped with a thermal conductivity detector. CO and H_2

production was quantitatively detected using a carboPlot P7 capillary column, 25 m in length and 25 μm in diameter. Temperature was held at 150 °C for the detector and 30 °C for the oven. The carrier gas was argon flowing at constant pressure of 0.5 bars. Injection was performed via a syringe (500 μL) previously degassed with CO_2. The retention time of CO was 1.44 min. Calibration curves for H_2 and CO were determined separately by injecting known quantities of pure gas.

Data Treatment of the Other Catalysts (Table 2)

In all cases, the cyclic voltammetric current (i)–potential (E) curves are approximately Nernstian:

$$i = \frac{i_{pl}}{1 + \exp\left[\frac{F}{RT}(E - E_{1/2})\right]},$$

with expressions of the plateau current i_{pl} and of the half-wave potential $E_{1/2}$,

$$i_{pl} = 2FS\sqrt{D_{cat}}\sqrt{k_1^{ap}[CO_2]}C_{cat}^0 \frac{1}{1 + \frac{\sqrt{k_1^{ap}[CO_2]}}{\sqrt{k_2^{ap}}\left(1 + \frac{\sqrt{k_2^{ap}}}{\sqrt{k_1^{ap}[CO_2]}}\right)}},$$

$$E_{1/2} = E_{cat}^0 + \ln\left\{1 + \frac{\sqrt{k_1^{ap}[CO_2]}}{\sqrt{k_2^{ap}}\left(1 + \frac{\sqrt{k_2^{ap}}}{\sqrt{k_1^{ap}[CO_2]}}\right)}\right\},$$

that reflect the occurrence of a two-electron, two-step (rate constants: k_1^{ap} and k_2^{ap}, respectively) process. It is observed that the half-wave potential $E_{1/2}$ is close, in all cases, to the standard potential of the wave where catalysis takes place, $E_{1/2} \approx E_{cat}^0$ (3). It follows that

$$i_{pl} = 2FS\sqrt{D_{cat}}\sqrt{k_1^{ap}[CO_2]}C_{cat}^0,$$

and that

$$TOF = \frac{TOF_{max}}{1 + \exp\left[\frac{F}{RT}(E - E_{1/2})\right]} \text{ with } TOF_{max} = k_1^{ap}[CO_2],$$

where TOF is turnover frequency, thus leading to the catalytic Tafel plots in Fig. 3 and the parameter values in Table 2.

1. Littler BJ, Miller MA, Hung C-H, Wagner RW, O'Shea DF, Boyle PD, Lindsey JS (1999) Refined synthesis of 5-substituted dipyrromethanes. *J Org Chem* 64:1391–1396.
2. Costentin C, Drouet S, Robert M, Savéant JM (2012) A local proton source enhances CO_2 electroreduction to CO by a molecular Fe catalyst. *Science* 338(6103):90–94.
3. Costentin C, Savéant J-M (2014) Multielectron, multistep molecular catalysis of electrochemical reactions: Benchmarking of homogeneous catalysts. *ChemElectroChem* 1: 1226–1236.